Wu Jie and New T.H. (2017) An investigation on supersonic bevelled nozzle jets. *Aerospace Science and Technology*, Vol. 63, pp. 278-293

An investigation on supersonic bevelled nozzle jets

Jie Wu[1,2] and T. H. New[1*]

[1]School of Mechanical and Aerospace Engineering, Nanyang Technological University
50 Nanyang Avenue, Singapore, 639798

[2]School of Aerospace Engineering, Huazhong University of Science and Technology
1037 Luoyu East Road, China, 430074

Abstract

This paper reports upon a numerical and experimental study on supersonic jets exhausting from bevelled nozzles with 30° and 60° exit inclination angles. To begin with, a simple but effective method to design a shock-free convergent-divergent circular jet nozzle to produce a well-conditioned supersonic Ma=1.5 jet based on simple circular fillets is presented. Subsequently Reynolds-Averaged Navier-Stokes simulations of circular non-bevelled and bevelled nozzle jets were performed at over-expanded, perfectly expanded and under-expanded conditions. Lastly, these supersonic jets were visualized experimentally using a modified Z-type Schlieren system. Results show that the shock cell structure within the jet potential core changes from a diamond pattern to triangular and rectangular patterns as the nozzle pressure ratio and inclination angle are varied. Furthermore, jet plumes are deflected differently when the bevelled nozzles were operated at off-design conditions, with changes to the supersonic jet potential core length. Finally, quantitative analysis of the results reveals that bevelled nozzles are able to reduce the intensity of the supersonic jet shock cell structure considerably, which is potentially useful for broadband shock-associated noise mitigation purposes.

Keywords*:* Supersonic jet; shock cell structure; bevelled nozzle; numerical simulation; Schlieren system

* Corresponding author – dthnew@ntu.edu.sg

Nomenclature

D	Diameter of the supersonic nozzle exit
Ma	Mach number
P	Pressure
T	Temperature
U	Velocity
x, y, z	Cartesian coordinates
γ	Specific heat ratio

Subscripts

d	Design condition
j	Jet flow condition
t	Total flow condition
amb	Ambient flow condition

Abbreviations

OASPL	Overall sound pressure level
RANS	Reynolds-Averaged Navier-Stokes
NPR	Nozzle pressure ratio
MOC	Method-of-characteristics
TKE	Turbulent kinetic energy

1. Introduction

Broadband shock-associated noise is one of the principle components of supersonic jet noise [1] and it is produced by the interactions between the large-scale turbulent jet flow structures

and the quasi-periodic shock cell structures when the supersonic jet is operated at off-design conditions. Through numerous experimental and numerical studies conducted in the past decades, the mechanism underpinning broadband shock-associated noise production by supersonic jets has been well documented [1-9]. It is generally agreed that this type of jet noise has a broad frequency range and the noise radiates towards the upstream direction. As such, a significant number of jet flow and noise control techniques have been proposed and explored to reduce such shock-associated jet noise. This includes making use of trailing-edge modifications [10-16], physical tabs [17, 18], fluid tabs [19-21], plasma actuators [22], elimination of Mach waves [23, 24], just to name a few. One of the most promising techniques involves careful modifications of the nozzle trailing-edges, due to their minimal impact upon jet thrust loss, and quite a number of studies had already been conducted to elucidate the more fundamental aspects of their implementations [25-29]. The motivations behind such modifications of the supersonic jet nozzles are two-fold - Firstly, they will alter the initial flow conditions at the nozzle exit as compared to a non-modified nozzle, which allows the manipulation of periodic shock cell structures within the supersonic jet potential core region [30]. Secondly, it has been observed previously that asymmetry in supersonic jet flows may disrupt screech feedback loop [31], with corresponding reductions in the screech amplitude. Therefore, noise mitigation using nozzle exit modifications appears to be an efficient approach in supersonic noise control and thus motivates the present study.

One of the earliest studies in supersonic jet noise reduction using bevelled nozzles was conducted by Norum [31], when it was demonstrated that asymmetric jet nozzles could lead to significant reductions in jet screech amplitude levels. Subsequently, Wlezien and Kibens [18] investigated the flow behaviour and acoustic emissions of supersonic jets issuing from bevelled and tabbed nozzles, where bevelled nozzles were observed to produce a higher

overall sound pressure level (OASPL) at an azimuthal angle of 90° with respect to the circular nozzle. On the other hand, the OASPL of the bevelled nozzle close to azimuthal angle of 0° and 180° were much lower. Rice and Raman [32, 33] conducted studies on supersonic rectangular bevelled jets and observed significant increases in high-frequency jet noise, even though peak mixing noise was reduced. It is worthwhile to point out that these findings were further numerically verified by Tam et al. [34]. More recently, Viswanathan and Czeth [12] and Viswanathan[13] reported that bevelled nozzles lead to significant noise reductions along azimuthal directions below the longer nozzle lips. Furthermore, Power et al. [35] studied the acoustic properties of military style supersonic bevelled nozzle jets and noticed that a noise reduction of 3~4 dB could be achieved along the peak emission direction aligned with the longer nozzle lip region. Aikens et al. [36] simulated bevelled nozzles through the use of large-eddy simulations and observed that they looked promising in terms of peak noise amplitude reductions along certain azimuthal locations. It should also be noted that a significant number of earlier investigations tend to focus upon the noise and pressure behaviour only, with the notable exception of Samimy et al. [14] where unique vortex structures and vortical behaviour induced by the modified nozzle trailing-edges were described significantly. As such, the question of how supersonic jets emanating from bevelled nozzles behave at different flow conditions (take for instance, due to nozzle pressure ratio variations) and how they may potentially affect broadband shock-associated noise, remain outstanding. Thus, detailed flow visualizations and numerical simulations were conducted here to further understand these relationships that underpin broadband shock-associated noise associated with bevelled nozzles.

In this paper, supersonic jets issuing from 30° and 60° bevelled nozzles were studied to investigate the influence of nozzle exit inclination upon the supersonic jet flow structures,

particularly the shock cell within the jet potential core, at over-expanded, perfect expanded and under-expanded conditions. The content of this paper is organized such that the design of the convergent-divergent circular nozzle used here will firstly be presented, before numerical simulation and experimental procedures used in the present study are introduced. This will be followed by discussions and analysis upon the qualitative and quantitative results obtained, before some key concluding remarks are highlighted.

2. Numerical and experimental procedures

2.1 Numerical simulation procedures

Numerical simulations were carried out via both axisymmetric-based and full 3D-based Reynolds-Averaged Navier-Stokes (RANS) techniques for mean flow field predictions, as the shock structures of the present supersonic jet flows can be considered to be a quasi-steady flow phenomenon. The requisite RANS numerical simulations were carried out using ANSYS CFX solver, which is capable of predicting both viscous and inviscid flows associated with complex geometries ranging from subsonic flow to supersonic flow regimes [37-39]. In the present study, a high-resolution advection scheme was used to capture the shock/expansion formations accurately, due to its stable nature in supersonic flow simulations. On the other hand, embedded shear stress transport (SST) turbulence model was employed for turbulence transport purposes in the governing equations, which has been found to be suitable for compressible flow simulations by Menter et.al [40, 41]. To better facilitate nozzle contour optimizations and flow comparisons, axisymmetric flow simulations were conducted before full 3D simulations were performed.

Two types of meshes were generated for axisymmetric and 3D numerical simulation models respectively. The axisymmetric mesh was primarily used for the fillet-nozzle optimization

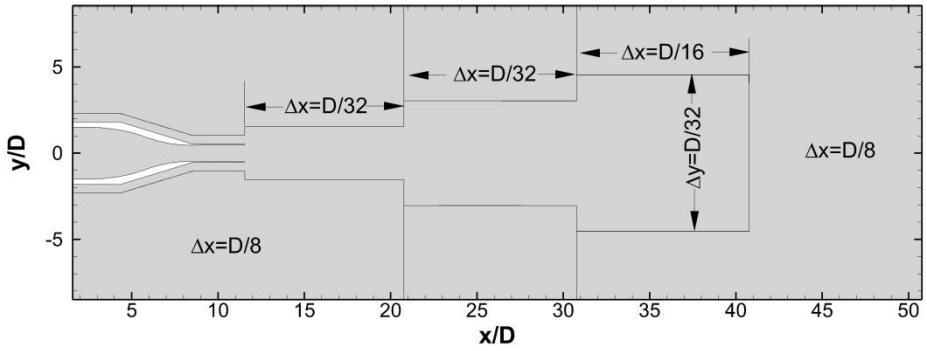

Fig. 1 Computational domain used in axisymmetric numerical simulations

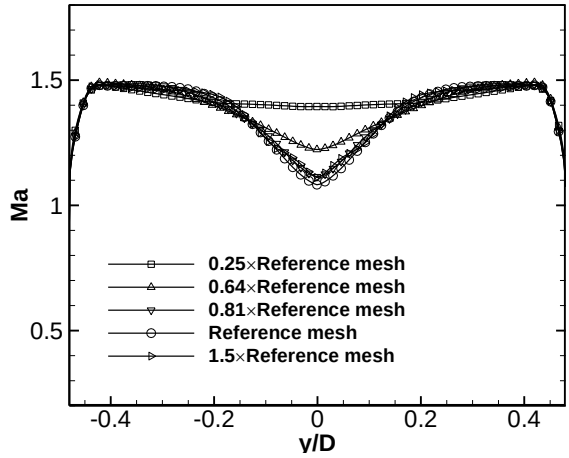

Fig. 2 Mesh independence check

stage, while the full 3D mesh was used for final validations and numerical results. All meshes were generated through ANSYS ICEM-CFD and the mesh density used in the present study adopted the recommended parameters suggested by [42, 43] to ensure adequate spatial accuracy for the present supersonic jet simulations. For the axisymmetric mesh, the computational domain covered 52D and 8.5D in the axial and radial directions respectively, as shown in Fig. 1. Mesh independence check had been performed by taking the mesh density in Fig. 1 as a reference, and compared to different mesh densities used in simulations for checking purposes. Subsequently, jet exit Mach number distributions were extracted from this series of simulations and presented in Fig. 2 for comparisons. As can be observed from the figure, the mesh density used in the present study proved to be sufficiently high for satisfactory convergence. Note that adaptive mesh refinement technique was not applied

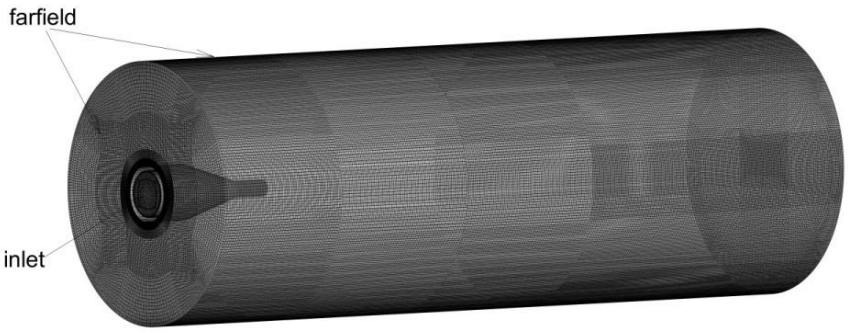

Fig. 3 Computational domain used in three-dimensional flow simulations

here as the growth of shear layer of the supersonic jet had been predicted based on experimental Schlieren images captured earlier by Wlezien and Kibens [18].

On the other hand, Fig. 3 shows the computational domain and meshing used for the full 3D simulations. Fine grid points were used for the supersonic nozzle section to capture the shock propagation whereas the grid points in the far field region were relatively coarse. This resulted in a total number of 19 million points for the 3D mesh. For the fillet-nozzle optimization simulations, the inlet total pressure and total temperature used were 8.3 bar and 300 K respectively, with a corresponding inlet velocity of 19 m/s at the inlet. Both internal and external nozzle walls were specified as non-slip adiabatic wall boundaries and the y^+ value adjacent to the walls was chosen to be 10. The far-field condition was chosen to one associated with an open ambient environment at one atmospheric pressure and the lateral side for the axisymmetric mesh was defined as a symmetry flow. Note that all the numerical simulations converged satisfactory with less than 1% change from iteration to iteration, as observed in the maximum supersonic jet Mach number.

2.2 Experimental setup and procedures

To validate the numerical simulations, experiment visualizations were performed using a modified Z-type Schlieren system. The Schlieren system included a 200W LED light source,

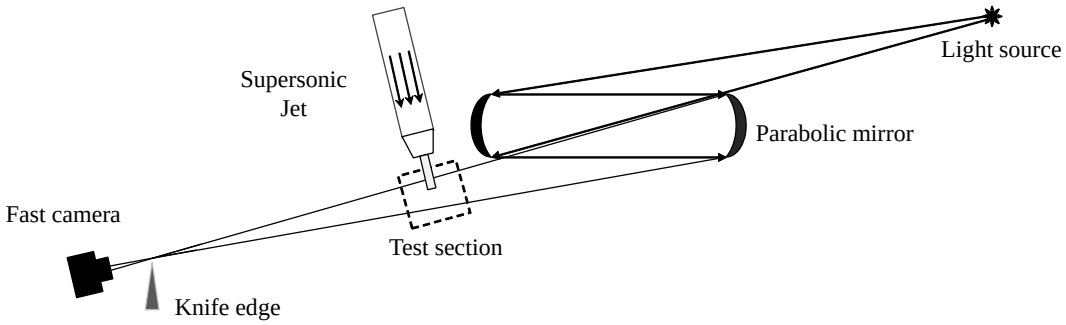

Fig. 4 Schematics of the modified Z-type Schlieren system

two 300 mm F/10 parabolic mirrors, a knife-edge and an IDT NX 4 high-speed CMOS camera. The 1024px × 1024px high-speed camera was used with a 105 mm, *f*2 Nikon lens and captured Schlieren images at a maximum frame rate of 1000 frames-per-second at full resolution. To capture the instantaneous transient jet flow behaviour, the exposure time of the camera was maintained at 1microsecond for all Schlieren visualizations. In a conventional Z-type Schlieren system, the distance between the two parabolic mirrors is supposed to be two times that of the parabolic mirror focal length [44], and the test section is generally located at the centre of the two parabolic mirrors. However, such a configuration was not suitable here since the jet flows would be in the optical paths several instances and produce sub-optimal Schlieren images.

As a result, a modified Z-type Schlieren was used instead, as shown in Fig. 4. The light source and the knife-edge were located at the focal points of the respective parabolic mirrors, such that the distance between the parabolic mirrors was reduced due to the collimated light between them. The jet nozzle was subsequently positioned between the camera and the second parabolic mirror for Schlieren visualizations. There are several advantages for such a Schlieren imaging setup: Firstly, the overall length of the Schlieren system was reduced. From the schematics, the maximum required distance of the modified Z-type Schlieren system is less than two times that of the parabolic mirror focal length. Secondly, such a setup

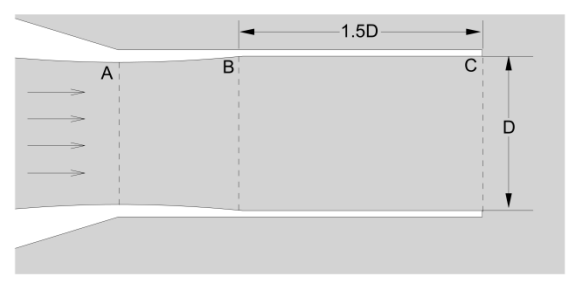

Fig. 5 Geometry of the initial non-optimized supersonic convergent-divergent nozzle

potentially offers much better Schlieren images as a result of the shorter distance between the camera and the jet nozzle, which will be desirable in terms of capturing detailed instantaneous supersonic flow structures. However, it should also be noted that the visualization region size is smaller for the present Schlieren system. Nevertheless, for the purpose of capturing good quality Schlieren images in the present study, this modified Schlieren system was found to be more than satisfactory.

2.3 Optimization of supersonic convergent-divergent nozzle contours

For the present study, a consistent supersonic convergent-divergent nozzle contour before the nozzle exit is necessary for both the numerical simulations and experiments for comparison purposes. Based on the current experimental jet apparatus, an initially non-optimized supersonic nozzle contour with convergent-divergent and straight sections is shown in Fig. 5, where the physical diameter of the nozzle exit is D=12.7 mm, location A is the sonic throat and B is the location where the nozzle area is designed to produce a nominal jet Mach number of 1.5. Note that the convergent-divergent section up to point B has been used in earlier supersonic jet studies [19]. Downstream of point B, a constant-diameter section BC of 1.5D length serves to extend the nozzle such that trailing-edge modifications can be implemented. The intention is to maintain a Mach number of 1.5 throughout section BC till the nozzle exit. Taking the initial physical configuration into consideration, it is clear that the lack of a smooth and appropriate expansion between sections AB and BC will produce

additional shocks within the supersonic nozzle, leading to possibly non-uniform flows within section BC.

As the present study needed to produce a uniform supersonic jet exit velocity of Ma=1.5, it is imperative that the transition between sections AB and BC is further modified to eliminate extraneous shocks within the nozzle. The most conventional way is to make use of Method-of-Characteristics (MOC) technique to design a transition with a contour that minimizes any shock productions. However, a satisfactory transition may also be generated from simple fillets with appropriate diameters and located at suitable locations. Thus, a comparison between jet flows resulting from transitions designed based on fillets with different diameters (i.e. 3.9D, 11.8D and 23.6D) and one based on MOC technique will be compared here, such that a suitable fillet-based transition would be selected for both experiments and numerical simulations. To incorporate a circular fillet such that it allows a smooth transition between sections AB and CD, a pre-determined fillet diameter would be chosen and then fitted to sections AB and CD contours such that both fillet end-lines meet the section contours tangentially. While the fillet centre point would vary with different fillet diameters used, the effects of fillet diameter in smoothing out the flow transitions are deemed to be more important for the present study.

3. Results and discussions

3.1 Filleted and MOC-optimized supersonic convergent-divergent nozzle contours

Numerical result obtained from an axisymmetric RANS simulation of a NPR=8.3 supersonic jet produced by the initially non-optimized nozzle is shown in Fig. 6. In order to highlight the extraneous shock waves produced by the imperfect inner nozzle contours, numerical Schlieren contours within the nozzle section are shown. It can be observed from the figure

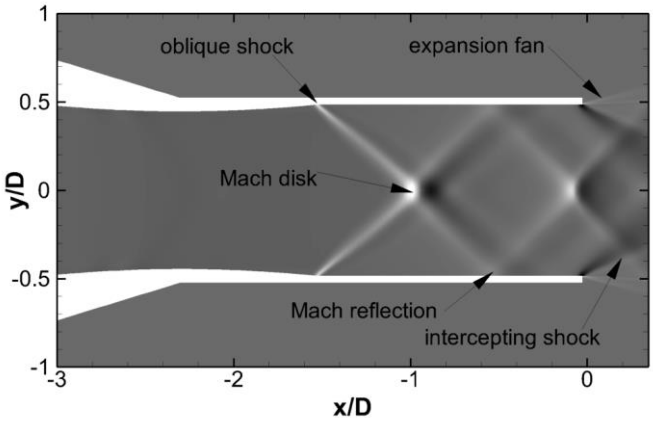

Fig. 6 Numerical Schlieren result for the initial non-optimized nozzle contour

that an under-expanded jet with internal shock diamond structures is produced, where the shock diamond originates from the junction between the expansion (i.e. AB) and constant diameter (i.e. BC) sections. Oblique shocks form at the junction due to the sudden compression and they intersect with each other to form the first Mach disk at approximately x/D=-1 location, before the shocks after the Mach disk reflect off the nozzle wall at x/D=-0.48 location. These reflected oblique shocks propagate further to form a second Mach disk at x/D=-0.08 location and pass through the intercepting shocks anchored at the nozzle exit lip.

Compared with conventional shock-free supersonic jet nozzles, the shocks originating from the inner wall of the nozzle section are clearly extraneous and undesirable. Not only do these shocks introduce inhomogeneity into the supersonic flow ahead of the jet nozzle exit, their interactions with the nozzle lip induce additional shocks as well. Such a non-uniform flow even before the jet exhausts fully from the nozzle will complicate studies associated with supersonic jet noise emissions, as the overall noise level of the supersonic jet is closely associated with the upstream conditions and shock wave structures within the jet potential core [45]. With this in mind, results associated with filleted and MOC-designed nozzles will be presented next to showcase the extent to which they are able to mitigate the above issues, as well as to point towards a suitable filleted nozzle design for the remaining study.

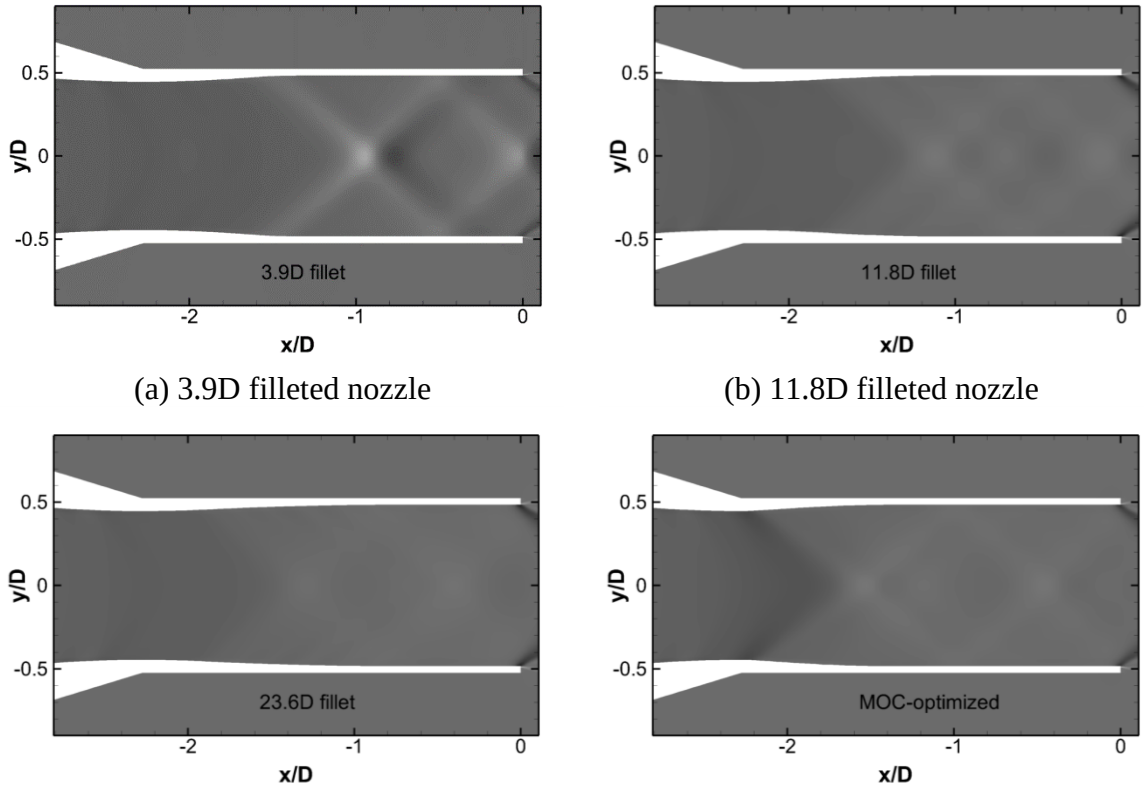

(a) 3.9D filleted nozzle (b) 11.8D filleted nozzle

(c) 23.6D filleted nozzle (d) MOC-optimized nozzle

Fig. 7 Numerical Schlieren results of filleted and MOC-optimized nozzles

Figure 7 shows the results obtained for supersonic jets issuing from nozzles modified with 3.9D, 11.8D and 23.6D fillets, as well as MOC-optimized nozzles. For the 3.9D fillet test case, little differences can be discerned between its flow field and that associated with the initially non-optimized nozzle, with the exception that the shock strengths are reduced significantly. This can be deduced from the colour of the shock structures (i.e. Figs. 6 and 7 use similar grayscale levels), where they are closer to the background colour. As the fillet diameter increases to 11.8D however, the compression waves between sections AB and BC are hardly visible and the associated shocks are now much weaker as compared to Fig. 6. To further mitigate the weak shocks that remain within the nozzle, the fillet diameter was increased to 23.6D. At first glance, it appears that the flow field does not differ from that associated with the 11.8D fillet. However, closer inspection of the inner nozzle region will reveal that the shocks are now diminished to an extent where the inner flow region can be

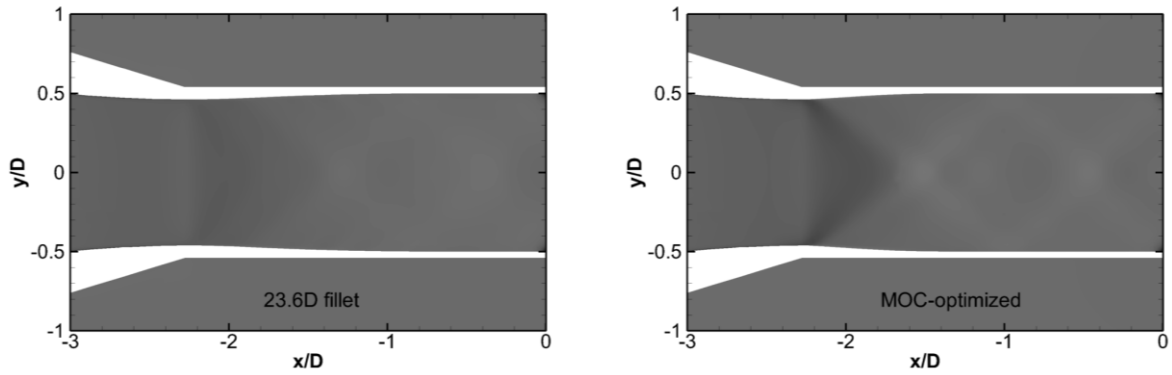

(a) (b)

Fig. 8 Numerical Schlieren results for the (a) 23.6D filleted nozzle and the (b) MOC-optimized nozzle, as determined from full 3D simulations

considered to be practically uniform. In particular, shock diamonds that were seen to originate from the inner nozzle wall previously do not seem to be present anymore. In fact, when the flow field result for 23.6D fillet is compared to that of the nozzle optimized through MOC technique as shown in Fig. 7(d), the 23.6D fillet case appears to lead to an even more uniform supersonic nozzle flow.

To further validate that the use of a 23.6D fillet is able to achieve a supersonic jet flow field that matches up with that produced by the MOC-optimized nozzle, as well as to address the uncertainties associated with the use of an axisymmetric model for the preceding simulations, additional validations will be performed based on full 3D simulations. As such, numerical Schlieren contours for both 23.6 filleted and MOC-optimized nozzles simulated fully in 3D are presented and compared in Fig. 8. Upon closer inspections, strong resemblances between Figs. 7(c), 7(d) and 8 can be readily observed. In fact, the 23.6D filleted nozzle can be seen to produce an even smoother expansion downstream of the throat region than the MOC-optimized nozzle. Furthermore, Figs. 9 and 10 show the jet velocity profiles and centreline velocity distributions for the non-optimized, 23.6D filleted and MOC-optimized nozzles, as determined from 3D simulations. The maximum velocity difference is estimated to be only

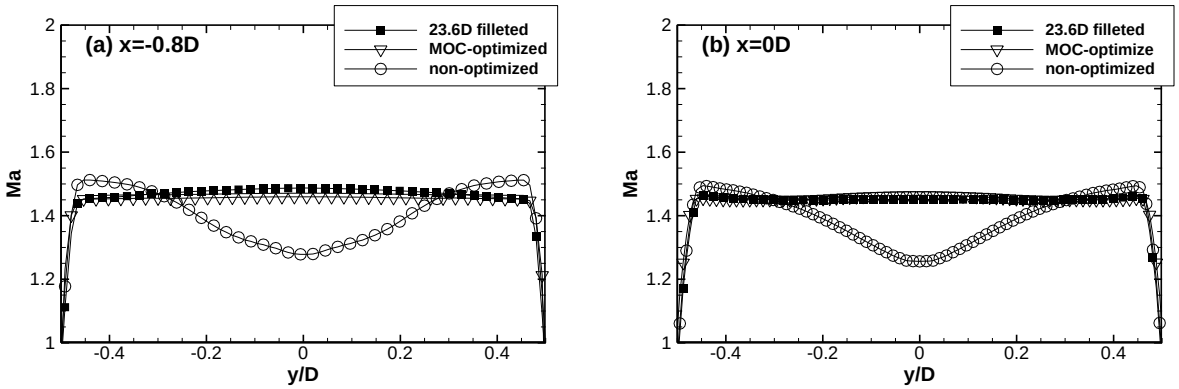

(a) (b)

Fig. 9 Jet velocity profile distributions at the (a) shock intersection and (b) nozzle exit locations for (i) non-optimized, (ii) 23.6D filleted and (iii) MOC-optimized nozzles, as determined from 3D simulations

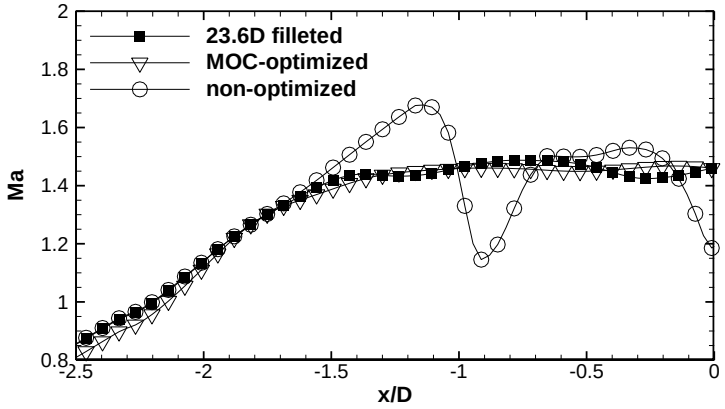

Fig. 10 Jet centreline velocity distributions for the (i) non-optimized, (ii) 23.6D filleted and (iii) MOC-optimized nozzles, as determined from 3D simulations

1.7% at x/D=-0.8 location and 0.9% at the nozzle exit for the cross-stream velocity profiles in Fig. 9. In addition, maximum velocity discrepancy in the jet centreline velocity distributions between the 23.6D filleted and MOC-optimized nozzles is about 2.7%, as shown in Fig. 10. Since satisfactory agreements in the velocity profiles between the 23.6D filleted and MOC-optimized nozzles can be seen in both axisymmetric and 3D simulations, the 23.6D filleted-nozzle was chosen as the circular baseline nozzle design. With that, bevelled nozzles were designed based on the same convergent-divergent configuration for the remaining study.

Table 1. Selected NPRs and corresponding jet Mach number

Ma_d	NPR	Ma_j	T_t
1.45	2.8	1.31	300
1.45	3.4	1.45	300
1.45	4.0	1.56	300
1.45	5.0	1.71	300

3.2 Non-bevelled and bevelled nozzle geometries

In the present study, four stagnation nozzle pressures of 2.8, 3.4, 4.0 and 5.0 bars were investigated and the definition of nozzle pressure ratio (NPR) is provided in Equation (1) as

$$NPR = \frac{P_t}{P_{amb}} = (1 + \frac{(\gamma - 1)}{2} Ma_j^2)^{\gamma/\gamma - 1}, \quad (1)$$

where *t* denotes stagnation flow condition and *amb* refers to ambient flow condition. The jet Mach numbers at different NPRs are listed in Table 1 above, where Ma_d is the nozzle design Mach number and *j* refers to the jet flow condition. Note that when the jet Mach number is smaller than the nozzle design Mach number, the jet flow at the nozzle exit would be over-expanded and vice versa. Since the computation mesh generation for the bevelled nozzles was carried out based on procedures similar to what was described previously, and that the numerical simulation procedures adopted remained the same with the exception of the incoming stagnation conditions presented in Table 1, these details will be omitted for the sake of brevity here.

Geometries of the three non-bevelled and bevelled test nozzles used for the numerical simulations and experiments are presented in Fig. 11. All of them incorporated the filleted convergent-divergent sections discussed in the previous section and the non-bevelled nozzle will be the baseline test case which comparisons will be carried out against. For the experiments conducted here, they were fabricated out of stainless steel blocks with the internal wall surfaces polished down to low roughness levels. The bevelled nozzles were

(a) (b) (c)

Fig. 11 Geometries of the (a) non-bevelled, (b) 30° bevelled and (c) 60° bevelled nozzles

fabricated based on the circular nozzle but with inclination angles of 30° and 60° with respect to the non-bevelled nozzle exit. All nozzles have a common exit diameter of 12.7 mm and possess similar mean heights such that they maintain a consistent coordinate system origin.

3.3 Mach number distributions and shock cell structures

Mach number distributions along the symmetry plane of the baseline nozzle are extracted from the 3D simulations and presented in Fig. 12. When NPR is 2.8, the nozzle exit pressure is lower than that of the ambient and the significant back pressure suppresses the jet expansion. This leads to two shocks originating from the nozzle lip that form a distinct Mach disk as they intercept each other. After the Mach disk, the shocks reflect multiple times within the jet potential core region to produce several discernible diamond shock cells. As the flow continues to propagate downstream, the shock cell structures within the potential core dissipate gradually and the jet shear layer merge at the end of the potential core region. As the NPR increases to 3.4, shock cells do not appear as a result of a perfect jet expansion. The length of the potential core can also be noted to increase by approximately 1.5D. At NPR=4.0, the shock cell structures reappear and the two shocks originating from the nozzle lip intercept each other to form a conventional diamond shock cell without a Mach disk. Additionally, the shock cell length is longer than that of the over-expanded case. When NPR is increased further to 5.0, the barrel shocks formed along the potential core are much more dominant due to the enhanced under-expansion scenario. In general, it can be observed that

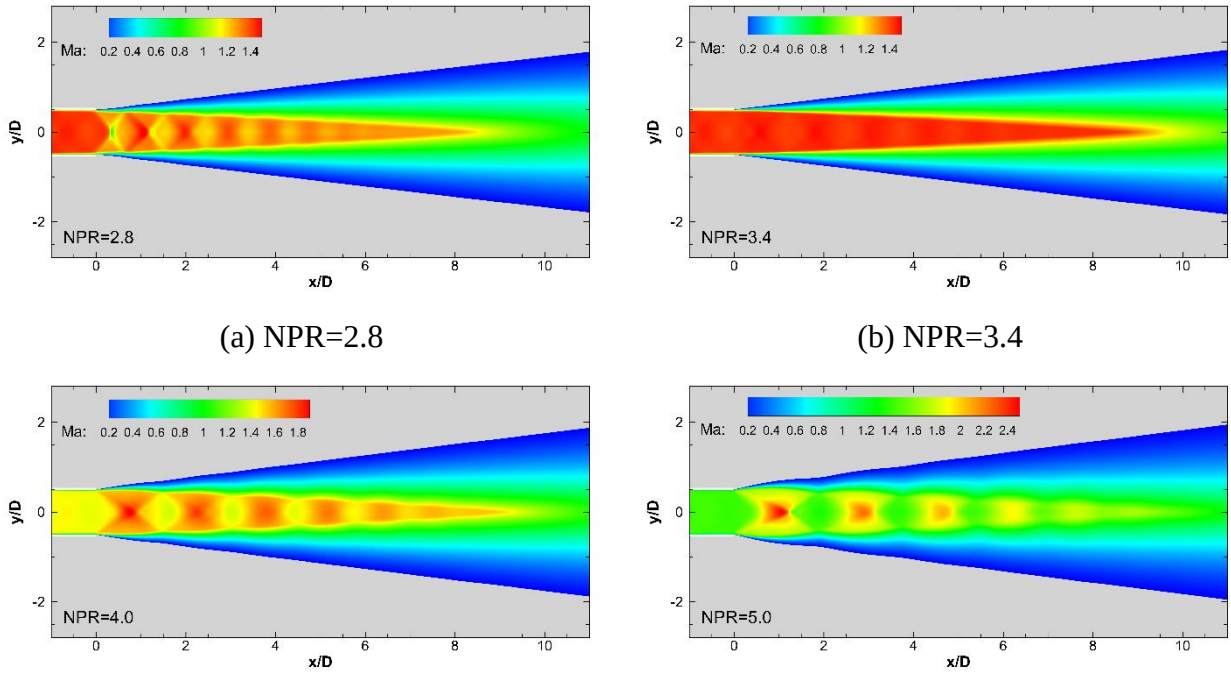

(a) NPR=2.8 (b) NPR=3.4

(c) NPR=4.0 (d) NPR=5.0

Fig. 12 Mach number distributions for the non-bevelled nozzle at (a) NPR=2.8, (b) NPR=3.4, (c) NPR=4.0 and (d) NPR=5.0

the shock cell length grows as the NPR increases, even though the length of the potential core seems invariant at both the perfectly expanded and under-expanded conditions.

Next, results for the 30° bevelled nozzle taken along its symmetry plane are presented in Fig. 13. In general, there exist several distinct flow differences as compared to the non-bevelled nozzle, particularly in terms of the shock cell pattern and jet plume deflection angle. The figure shows that when the NPR is 2.8, the shock cells take upon triangular shapes due to the asymmetric intercepting shocks resulting from the shorter and longer nozzle lengths. As the intercepting shock originating from the shorter nozzle lip reaches upon the longer nozzle lip, it encounters the intercepting shock forming off there. As a result, the intersection point of these two shocks is now significantly closer to the longer nozzle lip region and the intercepting shocks subsequently reflect within the jet potential core. This can be better appreciated in Fig. 13, where a close-up view of Fig. 13(a) also reveals the formation of a

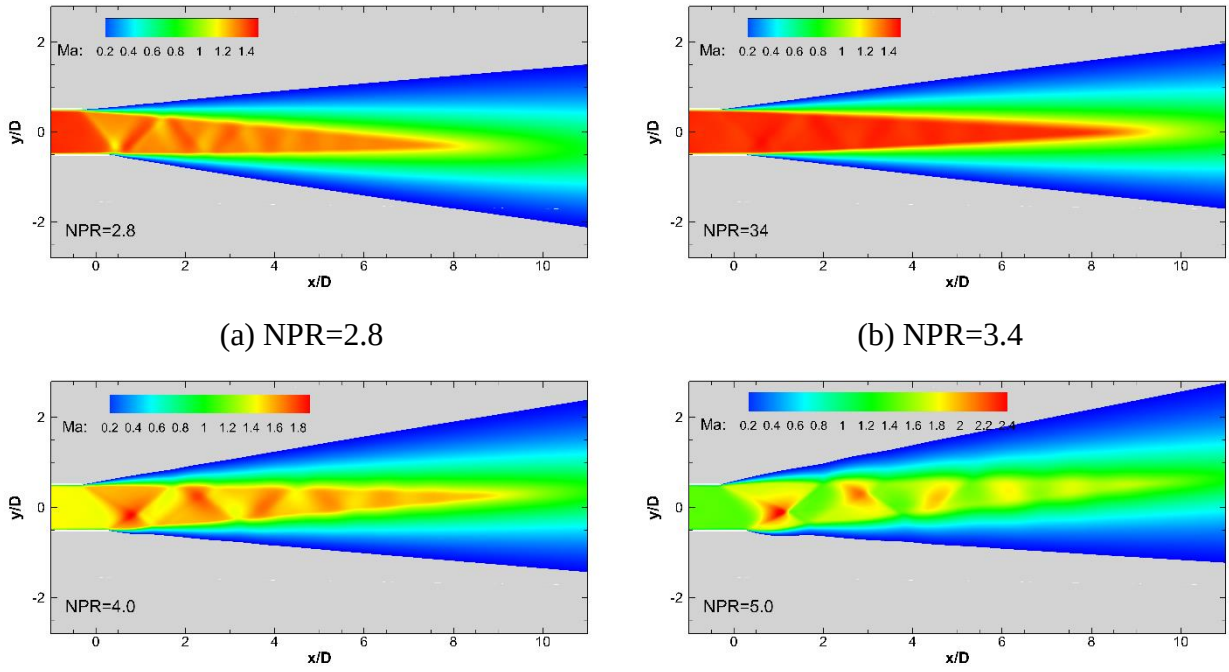

(a) NPR=2.8 (b) NPR=3.4

(c) NPR=4.0 (d) NPR=5.0

Fig.13 Mach number distributions for the 30° bevelled nozzle at (a) NPR=2.8, (b) NPR=3.4, (c) NPR=4.0 and (d) NPR=5.0, as taken along the symmetry plane

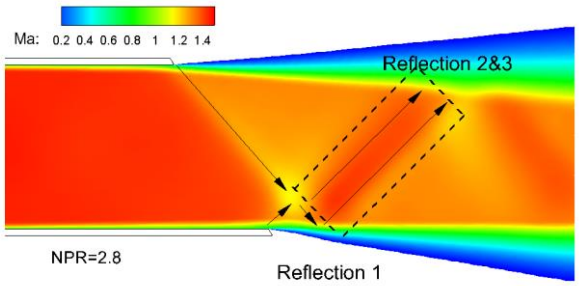

Fig.14 Shock interaction pattern for 30° bevelled nozzle at NPR=2.8

thin shock band, indicated in the region enclosed by the dashed lines in Fig. 14. Since the shock band thickness is relatively small, it would appear that the shock cell shape resembles a triangular shape. More interestingly, the resulting jet plume in Fig. 13(a) is observed to deflect towards the longer nozzle length direction. However, this is likely to be the result of a pressure relief lag between the shorter and longer nozzle lips, as described by Raman [35] and Rice and Raman [24, 25] previously.

When the NPR is increased to 3.4, the intercepting shocks disappear due to a perfectly-expanded jet flow scenario and differences in the nozzle lengths along this plane do not impact upon the Mach number distribution appreciably, as compared to the non-bevelled nozzle at the same NPR. When NPR is 4.0, the shock structures within the jet potential core appear to take on a rectangular shaped pattern. Intriguingly, the jet plume is now deflected towards the shorter nozzle length direction, opposite to what was observed at NPR=2.8. However, this can again be understood if one appreciates the fact that the intercepting shocks are less supressed at under-expanded conditions and as such, the first intersection point is displaced further downstream from the longer nozzle lip. Further downstream, the intersection point varies in position between the shorter and longer nozzle length regions, as the shocks get reflected within the jet potential core. Closer inspection shows that the shock interactions undergo similar behaviour as shown earlier in Fig. 14, except that the shock band is thicker now. As NPR finally reaches 5.0, not only are the shocks more dominant than before, the jet plume also incurs an even larger deflection towards the shorter nozzle length direction. Note that the jet potential core lengths along the symmetry plane are practically similar for the perfectly- and under-expanded cases.

As for the Mach number distributions along the plane orthogonal to the symmetry plane at different NPRs, Fig. 15 shows that the gross distributions are symmetrical like the non-bevelled nozzle. However, the shock cell structures are not very evident at an NPR of 2.8. Additionally, over-expanded conditions at NPR=2.8 produce a jet potential core length of approximately 6D, which is much shorter than that of the perfectly-expanded condition (i.e. NPR=3.4). On the other hand, diamond shock cells are prominent and jet potential core lengths are shorter at higher NPRs of 4.0 and 5.0, where under-expanded conditions prevail. However, these are most likely due to the jet plume deflections as observed in Fig. 13.

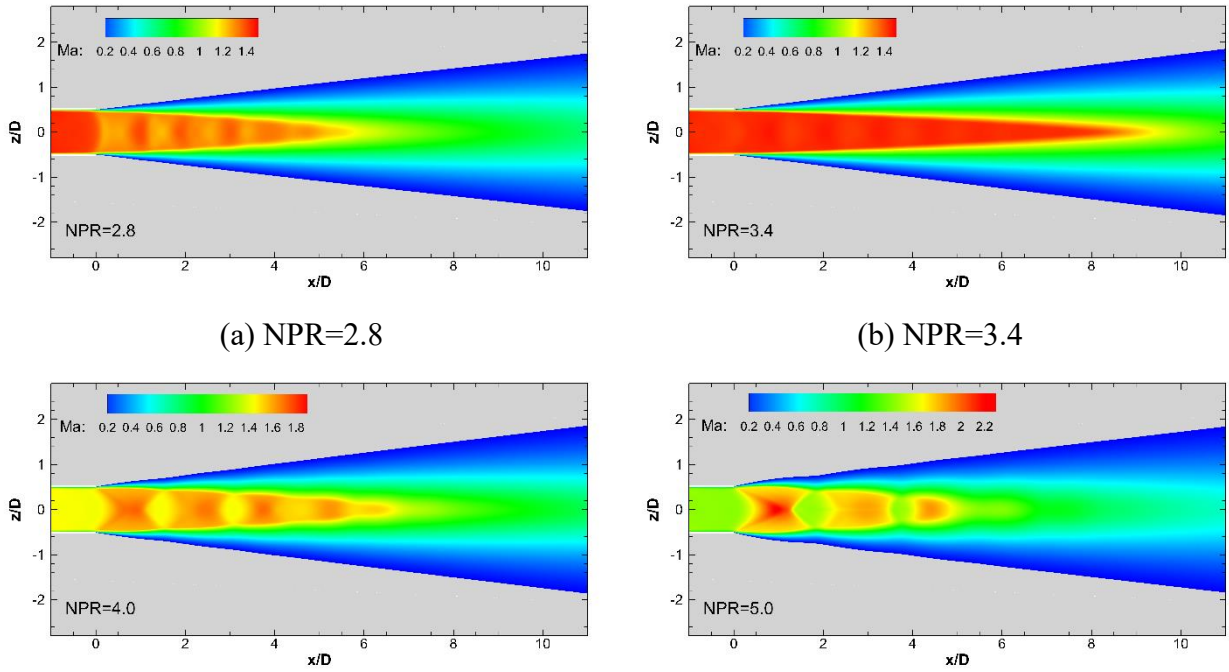

(a) NPR=2.8 (b) NPR=3.4

(c) NPR=4.0 (d) NPR=5.0

Fig. 15 Mach number distributions for the 30° bevelled nozzle at (a) NPR=2.8, (b) NPR=3.4, (c) NPR=4.0 and (d) NPR=5.0, as taken along the orthogonal plane

Correspondingly, Mach number distributions for the 60° bevelled nozzle along its symmetry plane are presented in Fig. 16. Compared to the 30° bevelled nozzle, the distance between the shorter and longer nozzle lips of the 60° bevelled nozzle is now much larger. When NPR is 2.8, the intercepting shock originating from the shorter nozzle lip is initially reflected by the longer nozzle lip wall first. Since the angle of incidence is small, the Mach reflection due to the jet shear layer close to the shorter nozzle lip is relatively weak. However, the intercepting shock from the longer nozzle lip is comparably more prominent and as the flow develops further downstream, this single shock is reflected within the jet potential core and produces triangular shock cell patterns. At NPR=3.4, the 60° bevelled jet is perfectly expanded and no shocks are produced. Since the flows along both the shorter and longer nozzle lips are balanced out by the ambient pressure, the jet potential core does not undergo any significant deflection.

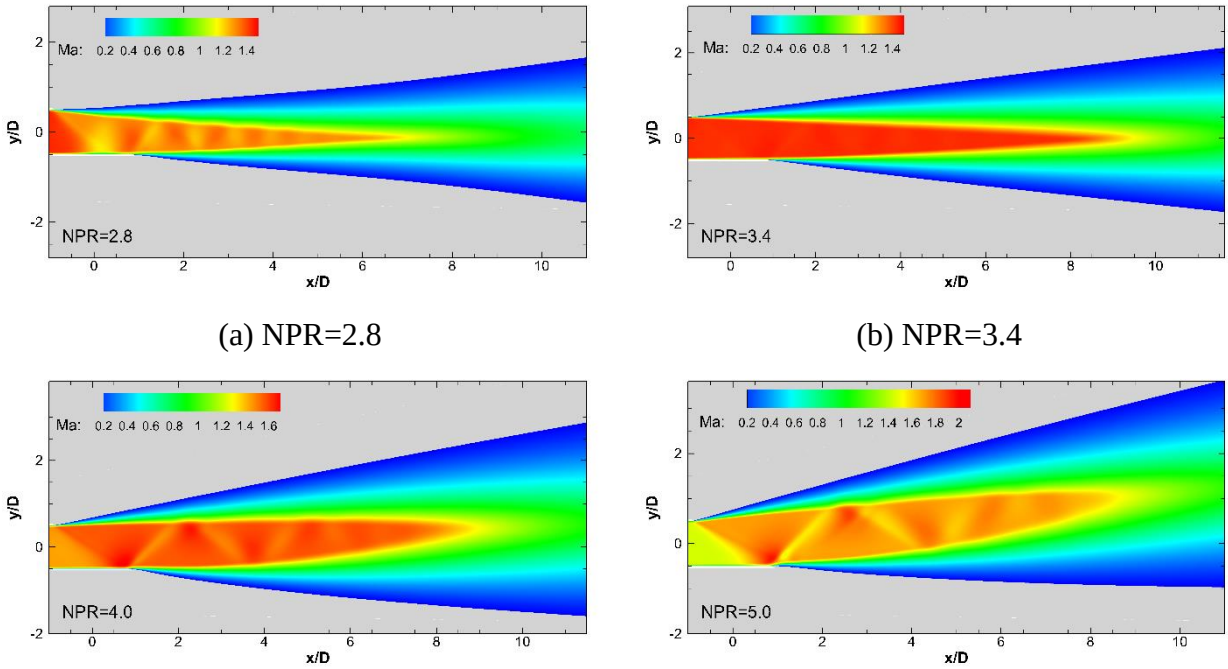

(a) NPR=2.8 (b) NPR=3.4

(c) NPR=4.0 (d) NPR=5.0

Fig. 16 Mach number distributions for the 60° bevelled nozzle at (a) NPR=2.8, (b) NPR=3.4, (c) NPR=4.0 and (d) NPR=5.0, as taken along the symmetry plane

When NPR is further increased to 4.0, the shock cells take upon a triangular pattern once again. In this case however, their formation mechanism is quite different from the aforementioned case at NPR=2.8. Instead, the intercepting shock generated from the shorter nozzle lip reaches the longer nozzle lip first, before it merges with another intercepting shock produced at the longer nozzle lip to produce a stronger single intercepting shock wave. Furthermore, the jet plume is deflected towards the shorter nozzle length direction as seen for the 30° bevelled nozzle previously at the same NPR, though the deflection angle appears to be larger for the 60° bevelled nozzle. When the NPR is 5.0, the shock cells are organized into triangular-like pattern again. It is interesting to note that, similar to the case of 30° bevelled nozzle at NPR=2.8, the intercepting shock generated by the shorter nozzle lip intersects with the shock originating at the longer nozzle lip such that the point of their intersection is relatively close to the longer nozzle lip region. Lastly, the jet plume deflection angle continues to increase at NPR=5.0, similar to the 30° bevelled nozzle.

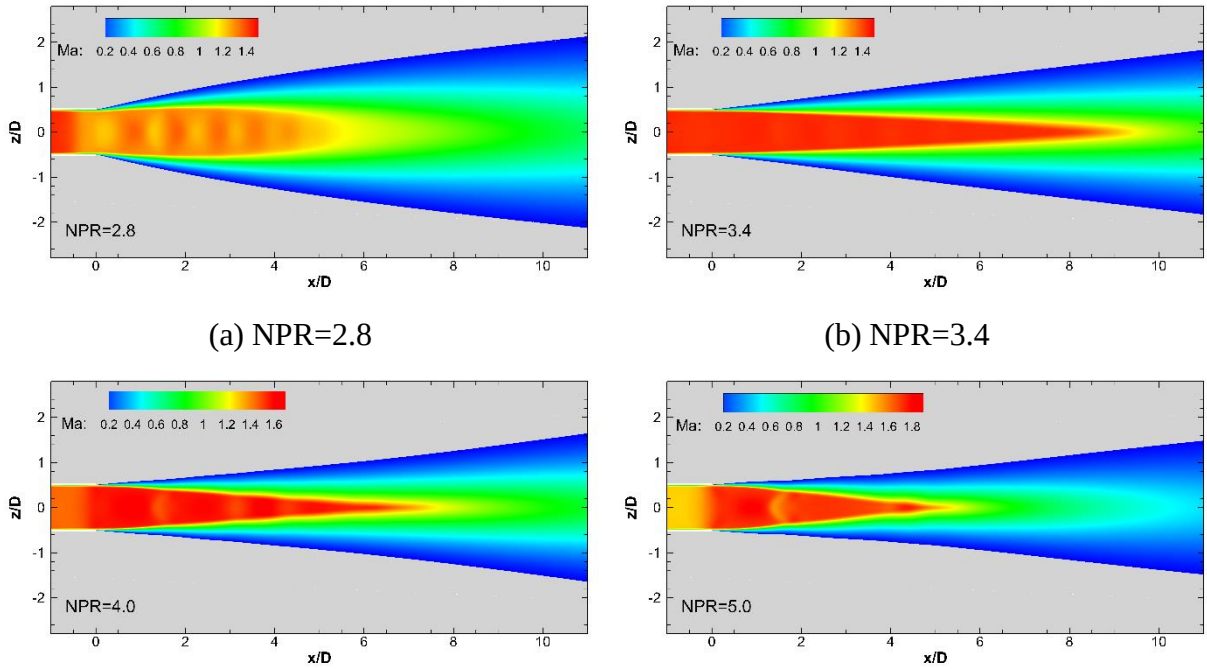

(a) NPR=2.8 (b) NPR=3.4

(c) NPR=4.0 (d) NPR=5.0

Fig. 17 Mach number distributions for the 60° bevelled nozzle at (a) NPR=2.8, (b) NPR=3.4, (c) NPR=4.0 and (d) NPR=5.0, as taken along the orthogonal plane

Lastly, along the plane orthogonal to the symmetry plane of the 60° bevelled nozzle as shown in Fig. 17, the shock structures are not too obvious at NPR=2.8. Similar situations exist at higher NPRs where the jet flows are under-expanded, which clearly deviate from the situation observed for the non-bevelled and 30° bevelled nozzles at the same NPRs. In addition, the jet potential core length decreases significantly as the NPR increases. Again, this can explain by the fact that the jet plume incurs increasingly larger deflections as the NPR increases, where the jet potential core moves further away from the jet centreline.

After presenting the flow field results along the two orthogonal planes, it will be timely to show the three-dimensional iso-Mach surfaces of the supersonic jet plumes in Fig. 18 for an overall appreciation of their three-dimensional flow behaviour. However, for the sake of brevity, only over- and under-expanded results at NPR=2.8 and 5.0 will be presented. It is clear from the cross-sectional results presented in the figure that the baseline nozzle produces

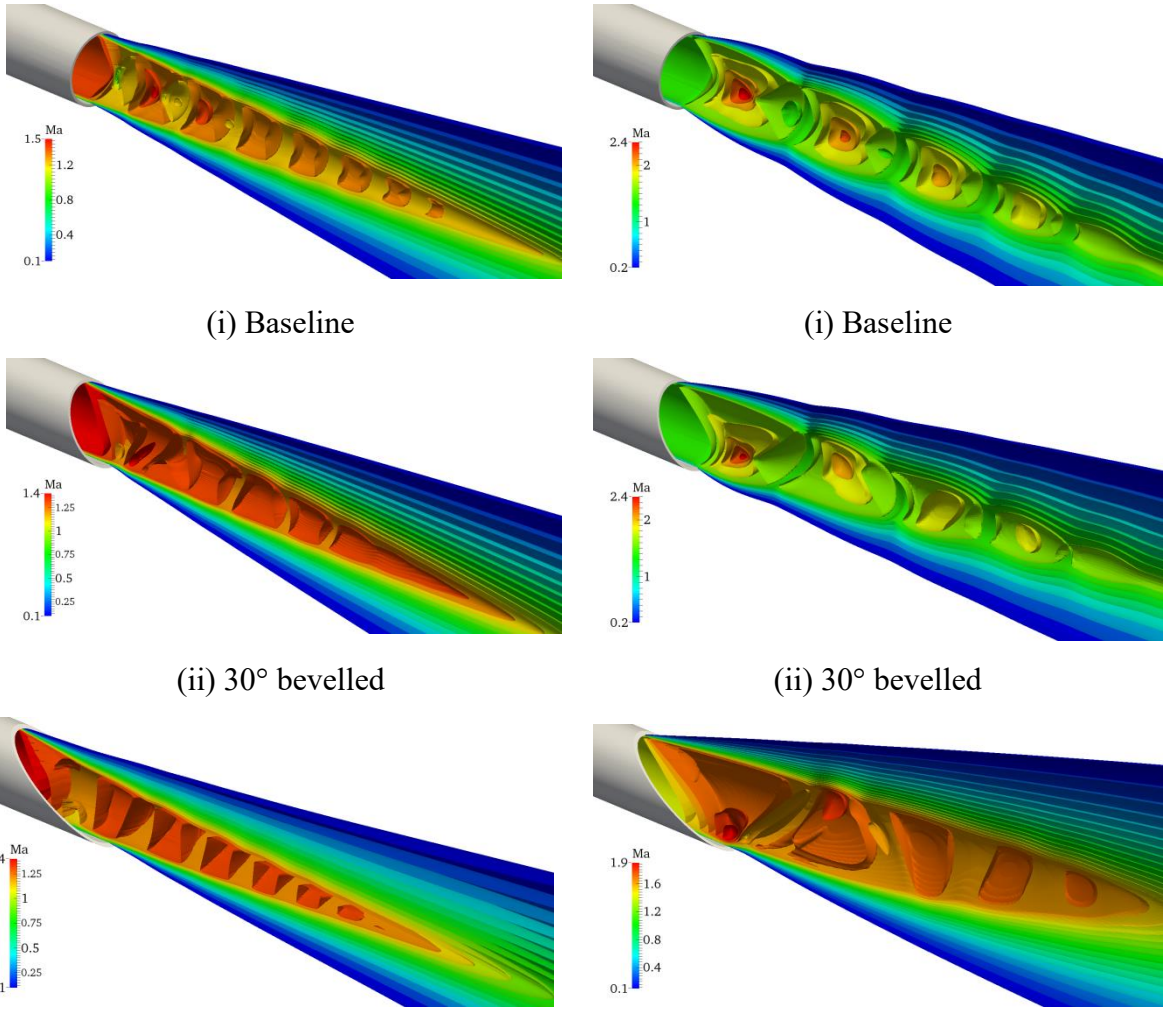

(i) Baseline (i) Baseline

(ii) 30° bevelled (ii) 30° bevelled

(iii) 60° bevelled (iii) 60° bevelled

(a) NPR=2.8 (b) NPR=5.0

Fig. 18 Cross-sectional iso-Mach surfaces of supersonic jet plumes for all three nozzle types at (a) NPR=2.8 and (b) NPR=5.0

axisymmetric shock structures, while bevelled nozzles produce asymmetric shock cells. This phenomenon is particularly more noticeable at under-expanded conditions at NPR=5.0. Greater jet plume deflection and distortions to the three-dimensional shock cell structures also occur at under-expanded conditions, which signify that a combination of large inclination angle and under-expanded conditions are necessary to exert more significant control over the supersonic jet plume behaviour.

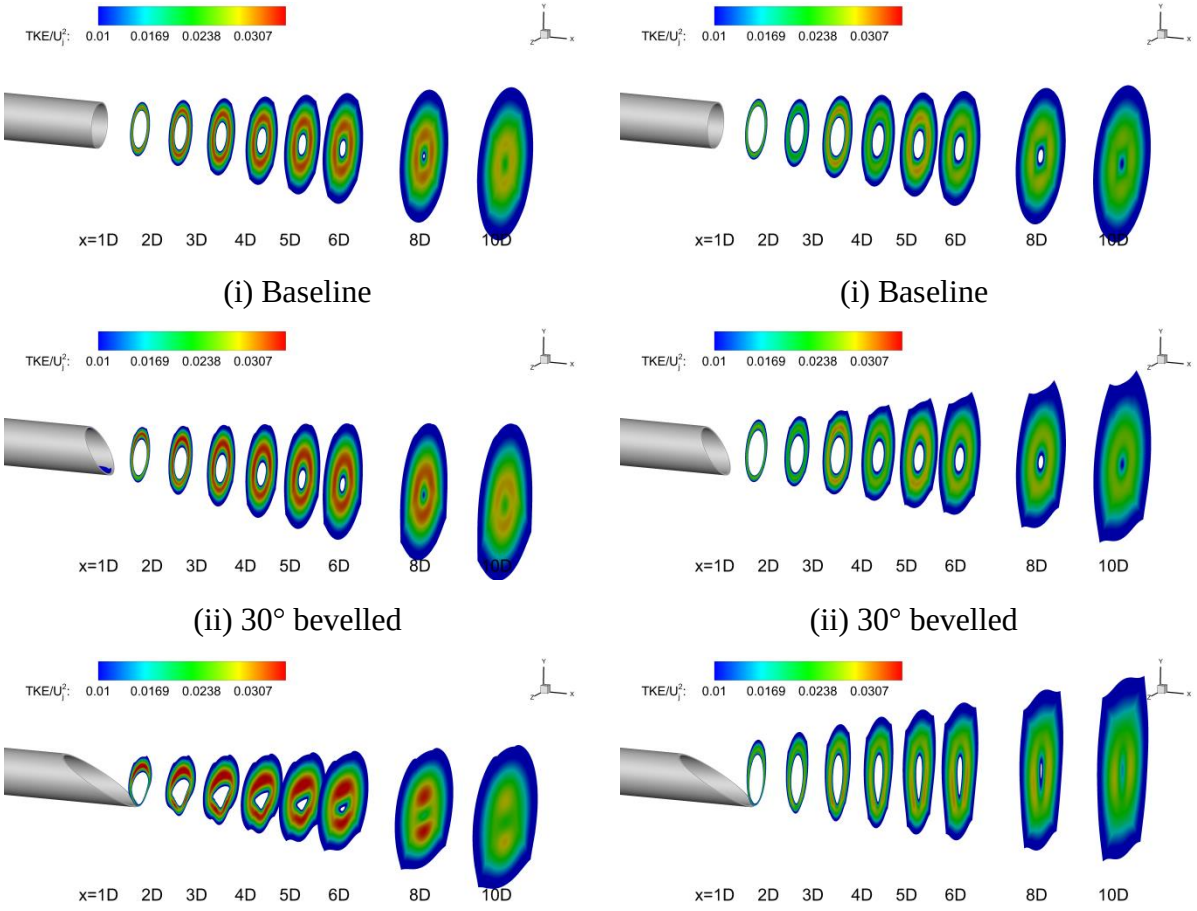

(i) Baseline (i) Baseline

(ii) 30° bevelled (ii) 30° bevelled

(iii) 60° bevelled (iii) 60° bevelled

(a) NPR=2.8 (b) NPR=5.0

Fig. 19 Cross-sectional normalized turbulent kinetic energy distributions for all three nozzle types at various downstream locations for (a) NPR=2.8 and (b) NPR=5.0

Finally, before the experimental Schlieren visualization results are presented in the next section, it will be informative to present the normalized turbulent kinetic energy (TKE) distributions associated with the three nozzle configurations studied here. Earlier studies have already indicated that modifying the nozzle lips geometrically could lead to a redistribution of the jet shear layer energy levels and Fig. 19 presents a comparison between cross-sectional TKE distributions at various downstream distances for the baseline and bevelled nozzles at NPR=2.8 and 5.0, based on an initial turbulence intensity level of 5% of the jet exit velocity. Since these NPRs are lower and higher than NPR=3.2 that is associated with a perfect expansion, the results in Fig. 19 not only allow good appreciation of the effects

of the NPR upon TKE distributions, but also shed light on how the TKE may be redistributed by using different bevelled nozzles at over-expanded and under-expanded conditions. For the baseline nozzle shown in Figs. 19(a)(i) and 19(b)(ii), it can be observed that the TKE are distributed in concentric rings initially for both over- and under-expanded conditions, before the they resemble square-like distributions closer to the jet core further downstream from x/D=8 location onwards.

In contrast, utilizing the bevelled nozzles can be seen to lead to increasingly asymmetric TKE distributions as the inclination angle increases, presumably due to the inclined vortices shed from the bevelled nozzle exits. For 30° bevelled nozzle at over-expanded condition, the TKE grows slightly fast along the longer nozzle lip even though the intensity of the TKE within the supersonic shear layer is lower than that along the shorter nozzle lip. However, at under-expanded condition, the TKE distribution is actually quite similar to that of the baseline nozzle. As the inclination angle increases to 60°, it is interesting to notice that higher TKE levels tend to be located along the shorter and longer nozzle lips at over- expanded condition, while they tend to be higher along the lateral sides of said nozzle lips at under-expanded condition. These observations are in agreement with earlier studies that had pointed out that it is possible to manipulate supersonic jet shear layer energy through relatively simple nozzle lip modifications.

3.4 Schlieren visualizations

Figure 20 shows the instantaneous Schlieren visualization images for the baseline non-bevelled nozzle at various NPRs. As the supersonic jet flow develops from over-expanded to under-expanded conditions, the intensity of the shocks increases (with the exception of the perfect expansion). This can be deduced from the increments in the first shock cell length and

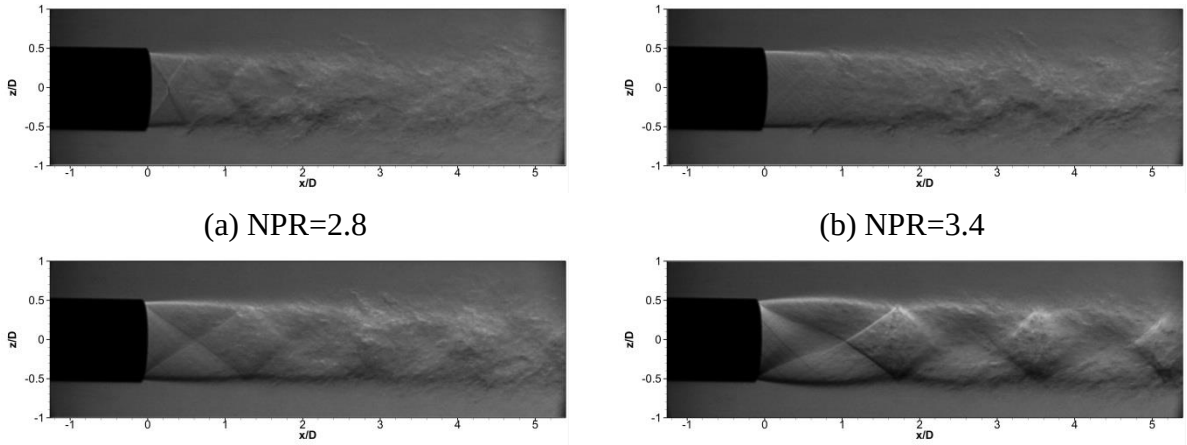

(a) NPR=2.8 (b) NPR=3.4

(c) NPR=4.0 (d) NPR=5.0

Fig. 20 Schlieren visualizations for the baseline non-bevelled nozzle

the number of visible shock cells. Due to the integration of density gradient by the Schlieren system, turbulent flow structures are generally dominant after two or three shock cells away from the nozzle exit. Nonetheless, the shock cell patterns and their lengths observed in these visualization images agree well with the numerical predictions presented earlier in Fig. 12.

Schlieren images taken for the 30° bevelled nozzle along the symmetry plane are presented in Fig. 21. When the NPR is 2.8, a triangular shock cell pattern is observed and the jet plume gets mildly deflected towards the longer nozzle lip direction. When the jet is supposedly to have expanded perfectly at NPR=3.4 however, very weak shocks emerge from both the shorter and longer nozzle lips, which may be attributed to slight inaccuracies in the supersonic jet stagnation pressure adjustments during the experiments. Nevertheless, as these shocks are very weak, they remain satisfactory for the purpose of validating the numerical simulation results. When the NPR is further increased to 4.0 and beyond, the shock cell pattern becomes rectangular-shaped and the jet plume deflects towards the shorter nozzle lip direction instead. These preceding observations are in-line with the numerical simulations presented in Fig. 13 earlier. Along the plane orthogonal to the nozzle symmetry plane as shown in Fig. 22, the flow behaviour is symmetrical about the jet centreline at all NPRs

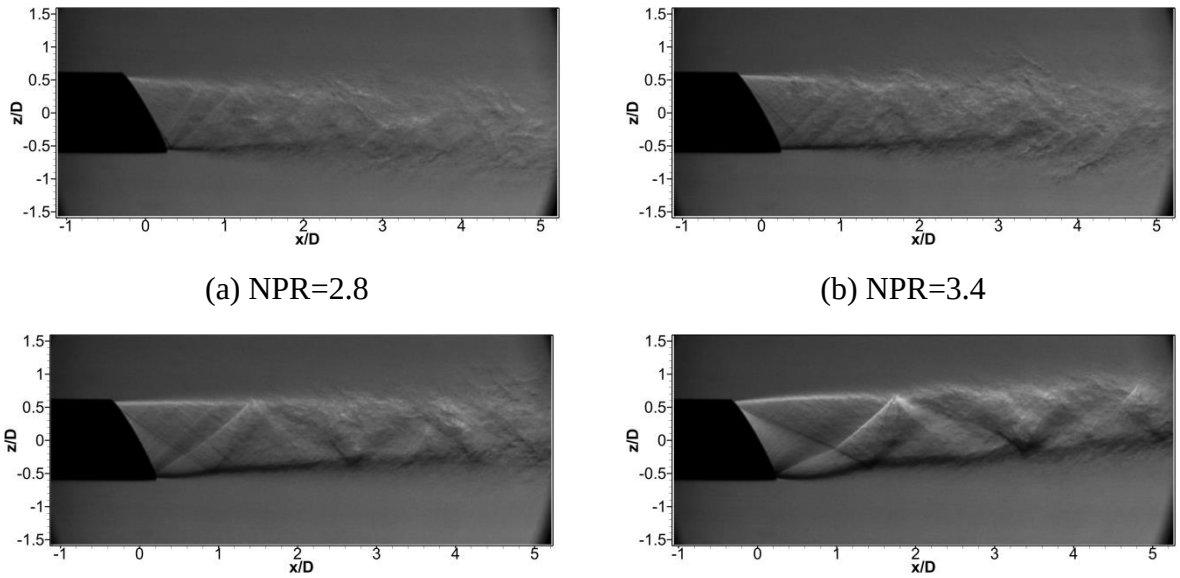

(a) NPR=2.8 (b) NPR=3.4

(c) NPR=4.0 (d) NPR=5.0

Fig. 21 Schlieren visualizations for the 30° bevelled nozzle along the symmetry plane

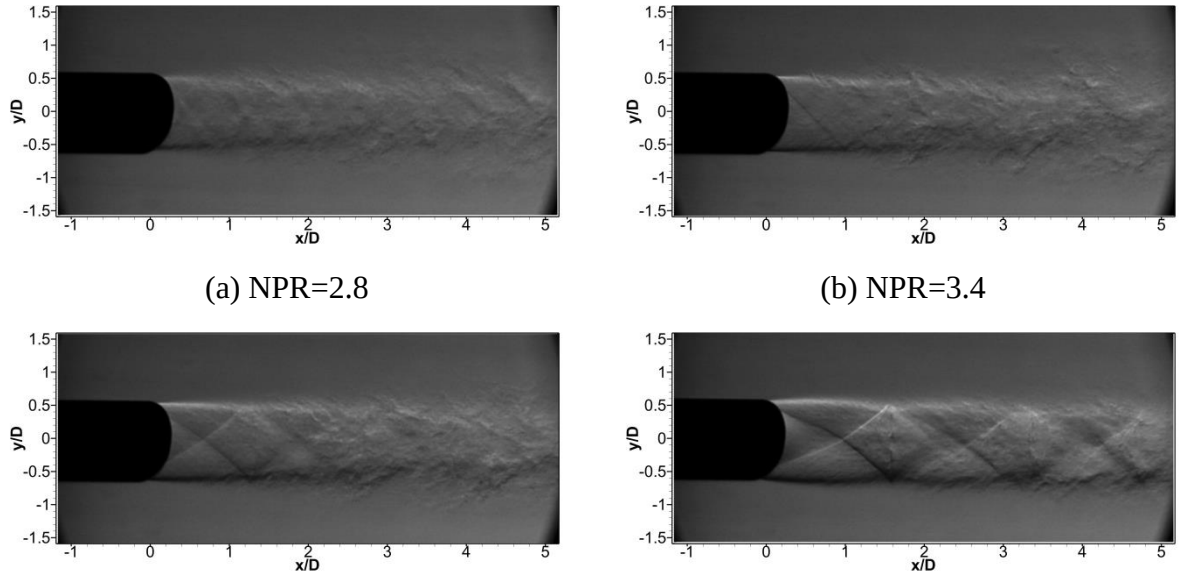

(a) NPR=2.8 (b) NPR=3.4

(c) NPR=4.0 (d) NPR=5.0

Fig. 22 Schlieren visualizations for the 30° bevelled nozzle along the orthogonal plane

studied. At NPR=2.8, the shock waves are hardly visible, though their intensity appears to increase correspondingly with NPR. In general, the shock structures and behaviour here are quite similar to that of the non-bevelled nozzle and agree well with numerical simulation results presented in Fig. 15.

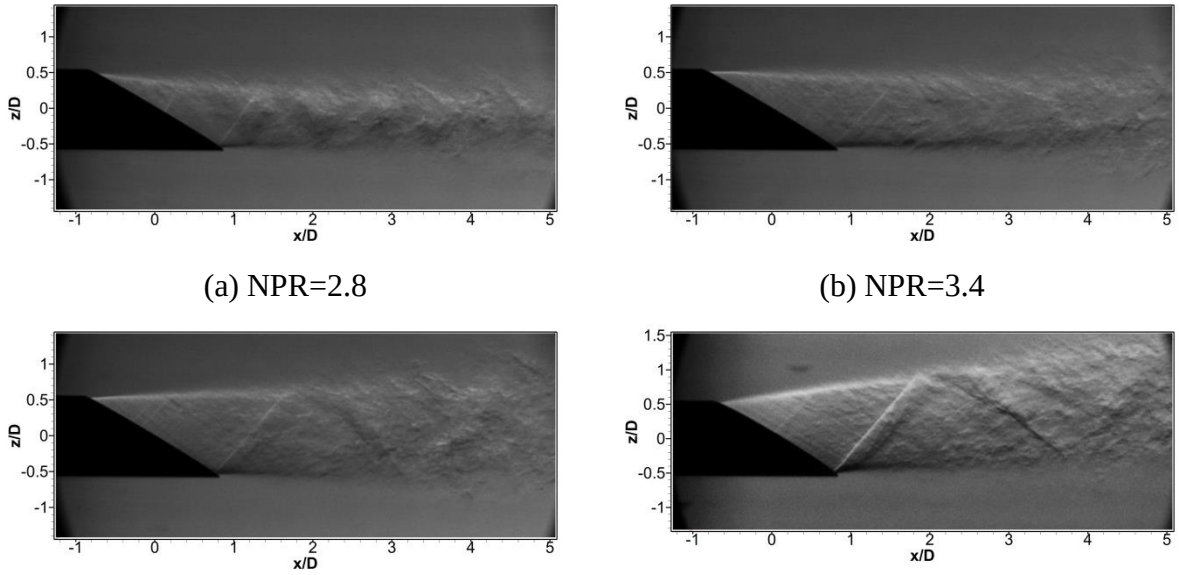

(a) NPR=2.8 (b) NPR=3.4

(c) NPR=4.0 (d) NPR=5.0

Fig. 23 Schlieren visualizations for the 60° bevelled nozzle along the symmetry plane

Moving on to the 60° bevelled nozzle, Fig. 23 shows Schlieren images taken along its symmetry plane. When the NPR is 2.8, the over-expanded jet plume produces two different branches of shock cell systems. The first branch is produced by the shorter nozzle lip, where it is reflected by the lower side of the bevelled nozzle wall before it reaches the longer nozzle lip region. On the other hand, the second branch is produced by the longer nozzle lip and the primary reason as to why shock cells take on a triangular-like pattern. For a perfectly expanded condition at NPR=3.4, only a very mild intercepting shock emerges from the longer nozzle lip. When the NPR increases further to NPR=4, a triangular shock cell is formed with a reduction in the number of visible shock cells as compared to the baseline nozzle. Schlieren images taken along the orthogonal plane for the same nozzle are presented in Fig. 24 and they generally indicate that the shock strengths are not as strong as those seen along the same plane for the non-bevelled and 30° bevelled nozzles earlier. Since they are in general agreement with the earlier numerical simulations, they will not be elaborated here for the sake of brevity.

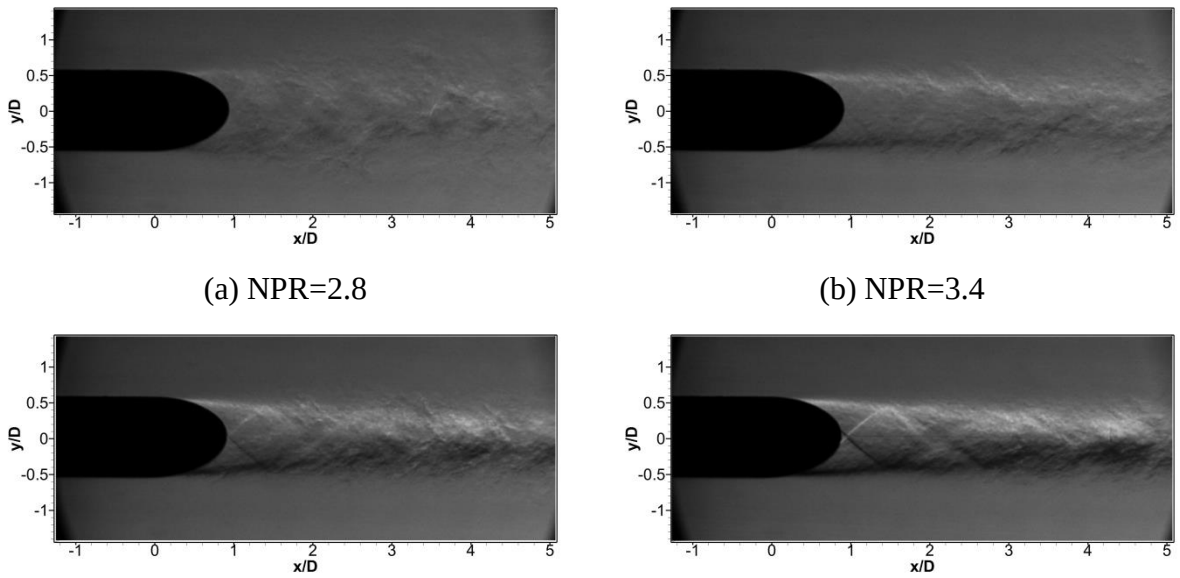

(a) NPR=2.8 (b) NPR=3.4

(c) NPR=4.0 (d) NPR=5.0

Fig. 24 Schlieren visualizations for the 60° bevelled nozzle along the orthogonal plane

To summarize, the experimental results are in good agreement with the numerical simulation results. Since the Schlieren results presented are instantaneous, turbulent flow structures with different length-scales can be observed and they may hinder clear visualizations of the visible shock cell numbers, with the exception of highly under-expanded cases. Nevertheless, shock structures within close proximity of the nozzle exits remain very discernible and demonstrate the ability of the present numerical simulations to replicate the experimental observations.

3.5 Quantitative analysis

To extract quantitative insights from the numerical simulation results, the jet plume deflection angles between the two bevelled nozzles were firstly extracted from the numerical simulation results and compared in Fig. 25. Note that negative and positive deflection angles denote deflections towards the shorter and longer nozzle lip direction respectively. In general, the figure demonstrates that the jet plume deflects downwards at over-expanded condition and upwards at under-expanded condition, regardless of the exact nozzle exit inclination angle. It can also be observed that the jet plume deflection angle is larger for the 30° and 60° bevelled

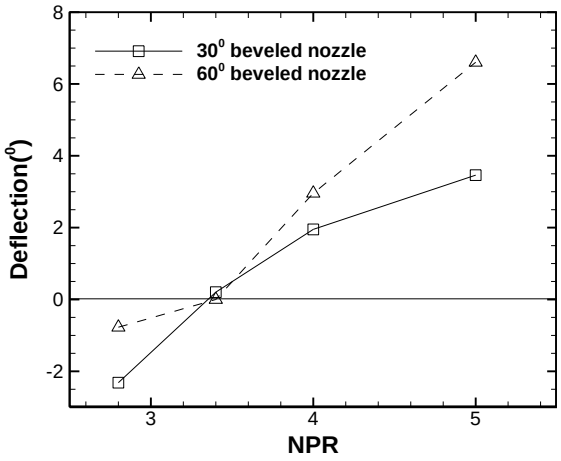

Fig. 25 Jet plume deflection angles for 30° and 60° bevelled nozzles

nozzles at over-expanded and under-expanded conditions respectively. Furthermore, the deflection angle varies in a relatively proportional manner with respect to NPR changes for both bevelled nozzles, which demonstrates potential for relatively straight-forward thrust or noise vectoring applications.

Next, jet centreline Mach number distributions are extracted from numerical simulation results and compared in Fig. 26. It should be mentioned that the centreline Mach numbers have been extracted along the direction of the deflected jet potential cores rather than along the nozzle centrelines to better highlight the changes associated with the main supersonic jet bodies. Interestingly, it can be observed that the jet potential core length for the 60° bevelled nozzle is almost always shorter than those for the other nozzles, regardless of whether the flow conditions are over- or under-expanded. Furthermore, Mach number fluctuations due to the presence of the shock waves for the bevelled nozzles are significantly smaller than those for the non-bevelled nozzle under off-design conditions, particularly for the 60° bevelled nozzle. According to the investigation on the relationships between the shock cell system and broadband shock noise carried out by Seiner and Norum [46], reduced shock cell strength (i.e. corresponding to smaller Mach number fluctuations here) may directly lead to a decrease

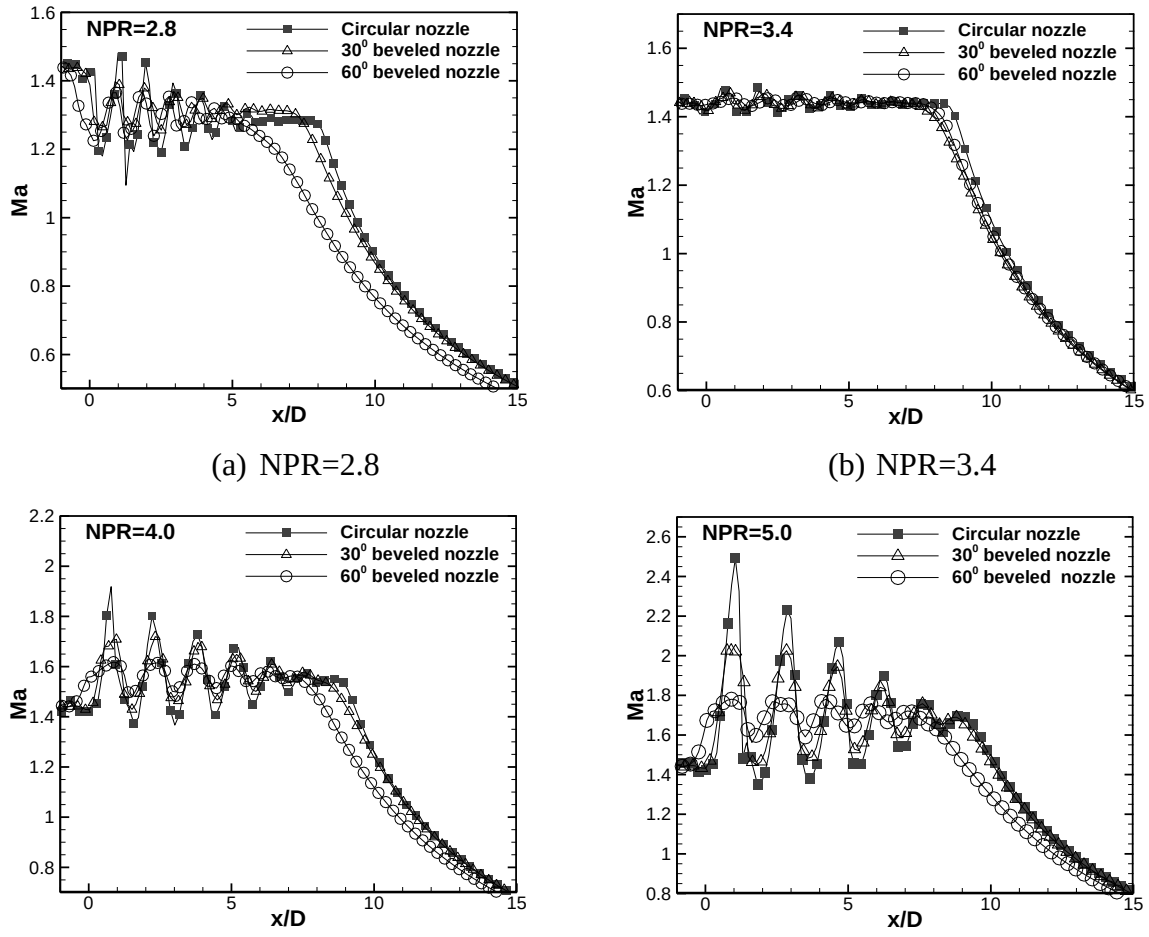

(a) NPR=2.8 (b) NPR=3.4

(c) NPR=4.0 (d) NPR=5.0

Fig. 26 Centreline Mach number distributions along the jet potential cores at (a) NPR=2.8, (b) NPR=3.4, (c) NPR=4.0 and (d) NPR=5.0

in supersonic jet broadband shock noise.

Additionally, shock cell lengths as a function of the nozzle exit geometry and NPR are compared in Fig. 27. Due to the significant production of turbulent flow structures within the jet potential core after one or two shock cells, only the first shock cell length will be compared here. It can be seen from the results that the numerical simulation results are in good agreements with the experimental visualizations. Furthermore, it would appear that the first shock cell lengths of both bevelled nozzles are quite similar to that of the non-bevelled nozzle at under-expanded conditions. On the other hand, the bevelled nozzles have longer

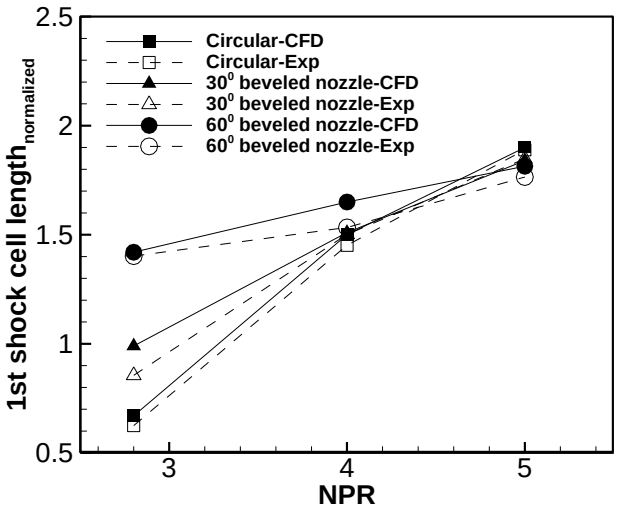

Fig. 27 Comparisons of first shock cell lengths between non-bevelled and bevelled nozzles

first shock cell lengths at over-expanded conditions. It is also worth noting that the first shock cell length for both bevelled nozzles increases as the inclination angle increases.

Finally, mass flow ratios estimated at different streamwise locations are determined for all test nozzles and presented in Fig. 28 to differentiate the mixing effects between the non-bevelled and bevelled nozzles. For the sake of brevity, the results are only shown for one over-expanded and one under-expanded condition at NPR=2.8 and 5.0 respectively. Note also that the mass fluxes are normalized by the nozzle exit jet mass flow. From the results, one can discern that the mass flux ratios for both bevelled nozzles do not deviate too much from that of the non-bevelled nozzle at both over-expanded and under-expanded conditions, except within the region between x/D=10 to 25. Within that region, both bevelled nozzles have slightly higher mass flux ratios and the exact inclination angle does not lead to any practical differences. These observations agree well with the experimental study conducted by Rice based on a relatively similarly-configured rectangular nozzle [32] and indicate that the bevelled nozzles does not enhance the mixing of the jet flows over the non-bevelled nozzle significantly. Instead, their primary flow influences consist of distortions to the shock

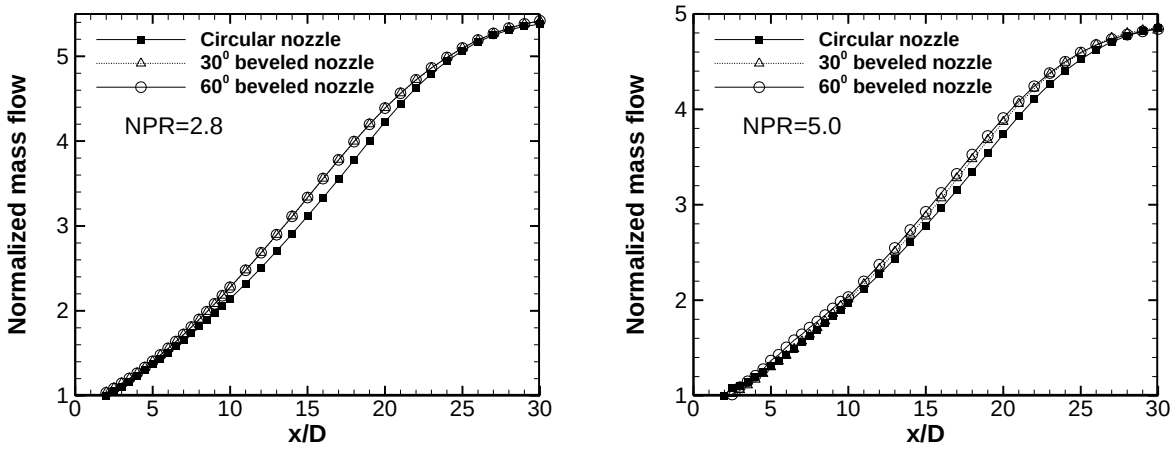

(a) NPR=2.8 (b) NPR=5.0

Fig. 28 Comparisons of mass flux ratios between non-bevelled and bevelled nozzles at over- and under-expanded conditions

cell formation characteristics and vectoring of the jet plume.

4. Conclusions

A numerical and experimental study on the shock cell structures and overall flow behaviour associated with Ma=1.5 supersonic jet issuing from 30° and 60° bevelled nozzles has been conducted and compared to a conventional non-bevelled nozzle. Optimization of the convergent-divergent (CD) section geometry to produce the desired initial supersonic jet flow conditions have also been elaborated, where axisymmetric and 3D numerical simulations demonstrate that incorporating a 23.6D fillet between the CD and straight nozzle sections produced supersonic jet flows comparable to that based on an MOC-optimized nozzle. Numerical simulation and experimental results agree well with each other, where the bevelled nozzles are observed to lead to shock cell structures that resemble triangular and rectangular patterns, unlike diamond shaped shock cells produced by the non-bevelled nozzle. Additionally, the bevelled nozzle jet plumes are observed to undergo systematic deflections induced by the pressure relief imbalance along the shorter and longer nozzle lip regions.

Generally speaking, the jet plume deflects towards the longer and shorted nozzle lip regions at over-expanded and under-expanded conditions respectively. Increasing either the NPR or nozzle inclination angle leads to larger jet plume deflections as well.

Mach number distributions taken along the deflected jet plume centrelines show that bevelled nozzles lead to shorter jet potential core lengths along the nozzle centreline, especially for the 60° bevelled nozzle. Fluctuations in these Mach number distributions have also been reduced for both bevelled nozzles and indicate weakened shock cell structures within the jet potential core region. Additionally, mass fluxes estimated at different streamwise locations suggest that bevelled nozzles do not lead to significant mixing enhancements between the jet flows and the ambient. Instead, collations between the results captured in the present study indicate that their primary effects lie in mitigating shock cell structure intensity levels, reducing jet potential core lengths and in particular, vectoring of the jet plume. As such, these insights provide valuable clues as to how shock-associated broadband noise levels in supersonic jets may be mitigated.

Acknowledgements

The authors gratefully acknowledge the support provided for the study through a Singapore Ministry of Education AcRF Tier-2 grant (Grant number: MOE2014-T2-1-002). Assistance from Professor D. Papamoschou at University of California, Irvine in providing the MOC-optimized supersonic convergent-divergent nozzle contour for comparisons here is also greatly appreciated. Lastly, valuable scientific discussions with Dr B. Zang and assistance provided by H. D. Lim, Xiaofeng Wei and U. S. Vevek are hereby acknowledged as well.

References

[1] C.K. Tam, Supersonic jet noise, Annual Review of Fluid Mechanics, 27 (1995) 17-43.

[2] J.M. Seiner, Advances in high speed jet aeroacoustics, in: 9th AIAA Aeroacoustics Conference, Williamsburg, Virginia, 15-17 Oct 1984, AIAA Paper 84-2275.

[3] J.M. Seiner, J.C. Manning, M.K. Ponton, Dynamic pressure loads associated with twin supersonic plume resonance, AIAA Journal, 26 (1988) 954-960.

[4] J.M. Seiner, D.K. McLaughlin, C.-H. Liu, Supersonic jet noise generated by large scale instabilities, NASA TP-2072, 1982.

[5] J. Panda, Shock oscillation in underexpanded screeching jets, Journal of Fluid Mechanics, 363 (1998) 173-198.

[6] G. Raman, Supersonic jet screech: half-century from Powell to the present, Journal of Sound and Vibration, 225 (1999) 543-571.

[7] S.A. Miller, The scaling of broadband shock-associated noise with increasing temperature, International Journal of Aeroacoustics, 14 (2015) 305-326.

[8] B. André, T. Castelain, C. Bailly, Broadband shock-associated noise in screeching and non-screeching underexpanded supersonic jets, AIAA Journal, 51 (2015) 665-673.

[9] C.W. Kuo, D.K. Mclaughlin, P.J. Morris, K. Viswanathan, Effects of jet temperature on broadband shock-associated noise, AIAA Journal, 53 (2015) 1515-1530.

[10] J.H. Kim, M. Samimy, Mixing enhancement via nozzle trailing edge modifications in a high speed rectangular jet, Physics of Fluids, 11 (1999) 2731-2742.

[11] C.W. Kuo, J. Veltin, D.K. McLaughlin, Advanced acoustic assessment of small-scale military-style nozzles with chevrons, in: 16th AIAA/CEAS Aeroacoustics Conference, Stockholm, Sweden, 07-09 Jun 2010, AIAA Paper 2010-3923.

[12] K. Viswanathan, M. Czech, Adaptation of the beveled nozzle for high-speed jet noise reduction, AIAA Journal, 49 (2011) 932-944.

[13] K. Viswanathan, Nozzle shaping for reduction of jet noise from single jets, AIAA Journal, 43 (2005) 1008-1022.

[14] M. Samimy, J.H. Kim, P. Clancy, Mixing enhancement in supersonic jets via nozzle trailing edge modifications, American Physical Society, Division of Fluid Dynamics Meeting, 1996.

[15] M. Samimy, P.S. Clancy, J.H. Kim, S. Martens, Passive control of supersonic rectangular jets via nozzle trailing-edge modifications, AIAA Journal, 36 (1998) 1230-1239.

[16] C.W. Kerechanin, M. Samimy, J.H. Kim, Effects of nozzle trailing edges on acoustic field of supersonic rectangular jet, AIAA Journal, 39 (2015) 1065-1070.

[17] M. Samimy, K. Zaman, M. Reeder, Effect of tabs on the flow and noise field of an axisymmetric jet, AIAA Journal, 31 (1993) 609-619.

[18] R. Wlezien, V. Kibens, Influence of nozzle asymmetry on supersonic jets, AIAA Journal, 26 (1988) 27-33.

[19] C. Wan, S. Yu, Investigation of air tab's effect in supersonic jets, Journal of Propulsion and Power, 27 (2011) 1157-1160.

[20] T.H. New, W. L. Tay, Effects of cross-stream radial injections on a round jet. Journal of Turbulence, 7 (2006) N57 1-20.

[21] P.J. Morris, D.K. Mclaughlin, C.W. Kuo, Noise reduction in supersonic jets by nozzle fluidic inserts, Journal of Sound & Vibration, 332 (2013) 3992-4003.

[22] M. Samimy, J.H. Kim, J. Kastner, I. Adamovich, Y. Utkin, Active control of high-speed and high-Reynolds-number jets using plasma actuators, Journal of Fluid Mechanics, 578 (2007) 305-330.

[23] D. Papamoschou, Mach wave elimination in supersonic jets, AIAA Journal, 35 (1997) 1604-1611.

[24] D. Papamoschou, New method for jet noise reduction in turbofan engines, AIAA Journal, 42 (2004) 2245-2253.

[25] T.H. New, D. Tsovolos, Influence of nozzle sharpness on the flow fields of V-notched nozzle jets, Physics of Fluids, 21 (2009) 084107.

[26] T.H. New, D. Tsovolos, On the vortical structures and behaviour of inclined elliptic jets, European Journal of Mechanics-B/Fluids, 30 (2011) 437-450.

[27] T.H. New, D. Tsovolos, On the flow characteristics of minor-plane inclined elliptic jets, Experimental Thermal and Fluid Science, 38 (2012) 94-106.

[28] T.H. New, H.M. Tsai, Experimental investigations on indeterminate-origin V-and A-notched jets, AIAA Journal, 45 (2007) 828-839.

[29] Shengxian Shi, T.H. New, Some observations in the vortex-turning behaviour of noncircular inclined jets, Experiments in Fluids, 54 (2013) 1614.

[30] E. Franquet, V. Perrier, S. Gibout, P. Bruel, Free underexpanded jets in a quiescent medium: A review, Progress in Aerospace Sciences, 77 (2015) 25-53.

[31] T. Norum, Screech suppression in supersonic jets, AIAA Journal, 21 (1983) 235-240.

[32] E.J. Rice, G. Raman, Supersonic jets from bevelled rectangular nozzles, in: Winter Annual Meeting of the ASME Symposium on Flow Acoustics Interaction and Fluid Control, New Orleans, Louisiana, Nov 28-Dec 03, 1993.

[33] E.J. Rice, G. Raman, Mixing noise reduction for rectangular supersonic jets by nozzle shaping and induced screech mixing, in: 15th AIAA Aeroacoustic Conference, Long Beach, California, 25-27 Oct 1993, AIAA Paper 93-4322.

[34] C.K. W. Tam, H. Shen, G. Raman, Screech tones of supersonic jets from bevelled rectangular nozzles, AIAA Journal, 35 (1997) 1119-1125.

[35] R. Powers, M. Senft, D.K. McLaughlin, Acoustics measurements of scale models of military style supersonic beveled nozzle jets, in: 17th AIAA/CEAS Aeroacoustics Conference (32nd AIAA Aeroacoustics Conference), Portland, Oregon, 05-08 Jun 2011, AIAA Paper 2011-2702.

[36] K.M. Aikens, G.A. Blaisdell, A.S. Lyrintzis, Analysis of converging-diverging beveled nozzle jets using large eddy simulation with a wall model, in:53rd AIAA Aerospace Sciences Meeting, Kissimmee, Florida, 5-9 Jan 2015, AIAA Paper 2015-0509.

[37] C. Ansys, ANSYS CFX-solver theory guide, ANSYS CFX Release, 2009.

[38] G. Aswin, D. Chakraborty, Numerical simulation of transverse side jet interaction with supersonic free stream, Aerospace Science and Technology, 14 (2010) 295-301.

[39] P. Cui, J. Han, Prediction of flutter characteristics for a transport wing with wingtip devices, Aerospace Science and Technology, 23 (2012) 461-468.

[40] F. Menter, M. Kuntz, R. Langtry, Ten years of industrial experience with the SST turbulence model, in: Proceedings of 4th International Symposium on Turbulence, Heat and Mass Transfer, Antalya, Turkey, 12-17 October, 2003. pp. 625–632.

[41] F.R. Menter, Review of the shear-stress transport turbulence model experience from an industrial perspective, International Journal of Computational Fluid Dynamics, 23 (2009) 305-316.

[42] H. Shen, C.K. W. Tam, Numerical simulation of the generation of axisymmetric mode jet screech tones, AIAA Journal, 36 (1998) 1801-1807.

[43] V. Vuorinen, J. Yu, S. Tirunagari, O. Kaario, M. Larmi, C. Duwig, B. Boersma, Large-eddy simulation of highly underexpanded transient gas jets, Physics of Fluids, 25 (2013) 016101.

[44] G.S. Settles, Schlieren and shadowgraph techniques: visualizing phenomena in transparent media, Berlin: Springer , 2001.

[45] J. Panda, An experimental investigation of screech noise generation, Journal of Fluid Mechanics, 378 (1999) 71-96.

[46] J.M. Seiner, T.D. Norum, Aerodynamic aspects of shock containing jet plumes, in: AIAA 6th Aeroacoustics conference, Hartford, Connecticut, 04-06 Jun 1980, AIAA Paper 80-0965.